

Localization and Impact of Pb-Non-Bonded Electronic Pair on the Crystal and Electronic Structure of Pb_2YSbO_6

Sebastián A. Larrégola,^{*,†} José A. Alonso,[‡] Victor A. de la Peña-O'Shea,[§] Denis Sheptyakov,^{||} Vladimir Pomjakushin,[⊥] María T. Fernandez-Díaz,[#] and José C. Pedregosa[†]

[†]Instituto de Investigaciones en Tecnología Química (INTEQUI), Universidad Nacional de San Luis - CONICET, Chacabuco y Pedernera, 5700 San Luis, Argentina

[‡]Instituto de Ciencia de Materiales de Madrid, C.S.I.C., Cantoblanco, 28049 Madrid, Spain

[§]Thermochemical Processes Unit, IMDEA Energy Institute, c/Ramón de la Sagra 3, Parque Tecnológico de Móstoles, 28935 Móstoles, Madrid, Spain

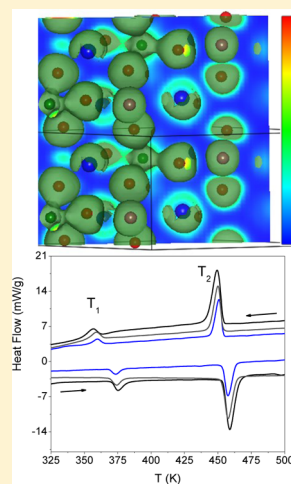
^{||}Laboratory for Neutron Scattering, ETH Zurich and PSI Villigen, CH-5232 Villigen PSI, Switzerland

[⊥]Paul Scherrer Institute, WHGA/133, 5232 Villigen PSI, Switzerland

[#]Institut Max Von Laue Paul Langevin, F-38042 Grenoble, France

Supporting Information

ABSTRACT: The synthesis and crystal structure evolution of the double perovskite Pb_2YSbO_6 is reported for the first time. The structure has been analyzed in the temperature range between 100 and 500 K by using a combination of synchrotron and neutron powder diffraction. This compound shows two consecutive first order phase transformations as previously observed for a subgroup of Pb_2RSbO_6 perovskites ($R = \text{rare earths}$). The thermodynamic parameters associated with the phase transitions were calculated using differential scanning calorimetry (DSC), and the role of the diverse cations of the structure was studied from DFT calculations for the room temperature polymorph. The crystal structure evolves from a $C2/c$ monoclinic structure ($a^-b^-b^-$ tilting system in Glazer's notation) to another monoclinic $P2_1/n$ ($a^-a^-b^+$) phase with an incommensurate modulation and finally to a cubic $Fm\bar{3}m$ perovskite ($a^0a^0a^0$). The highly distorted nature of the room temperature crystal structure seems to be driven by the polarization of the Pb lone pair which shows a marked local effect in the atomic spatial arrangements. Moreover, the lone pairs have been localized from DFT calculations and show an antiferroelectric ordering along the b monoclinic axis.



INTRODUCTION

Double perovskites $\text{A}_2\text{B}'\text{B}''\text{O}_6$ have aroused great interest to materials physicists and chemists in the past years due to the great variety of interesting physical properties they exhibit such as superconductivity,^{1,2} dielectric properties,^{3,4} magnetoresistance,^{5,6} etc. The crystal structures present a three-dimensional framework of corner-sharing $\text{B}'\text{O}_6$ and $\text{B}''\text{O}_6$ octahedra where the A cations occupy the voids between every eight octahedra, in an ideal AO_{12} coordination.

The great number of chemical substitutions that these compounds admit generates small distortions depending on the bond length ratio. Taking this into account, Goldschmidt defined in 1926 a geometrical parameter named tolerance factor⁷ that involves the main perovskite bond lengths as

$$t = \frac{\langle \text{A}-\text{O} \rangle}{\sqrt{2} \cdot \langle \text{B}-\text{O} \rangle} \quad (1)$$

Here the bond lengths can be calculated from the ionic radii of A, B, and O species (for instance those tabulated by Shannon⁸),

at ambient pressure and room temperature. $\langle \text{B}-\text{O} \rangle$ is the average between $\text{B}'-\text{O}$ and $\text{B}''-\text{O}$ bond lengths in a $\text{A}_2\text{B}'\text{B}''\text{O}_6$ -type perovskite.

A measure of the mismatch of the average $\langle \text{A}-\text{O} \rangle$ and $\langle \text{B}-\text{O} \rangle$ equilibrium bond lengths in the cubic phase is given by the deviation from unity of the tolerance factor. Since the $(\text{A}-\text{O})$ and $(\text{B}-\text{O})$ bonds have different thermal expansion and compressibility, $t = t(T, P)$ is unity only at a single temperature for a given pressure. A larger thermal expansion of the $(\text{A}-\text{O})$ bonds makes $dt/dT > 0$ except where a localized to itinerant transition occurs.⁹ Normally the $(\text{A}-\text{O})$ bond is more compressible than the $(\text{B}-\text{O})$ bond,^{10–12} which makes $dt/dP < 0$. In this way, if $t < 1$, the $\text{B}-\text{O}$ bonds are under compression while the $\text{A}-\text{O}$ bonds are under tension. The structure alleviates these stresses by a cooperative rotation of the BO_6

Received: February 13, 2014

Published: May 13, 2014

octahedra that lowers the space group symmetry from the cubic ($Fm\bar{3}m$).

The most commonly observed distortions in perovskites are the ones driven by the tilting of the octahedra, which can give rise to different symmetries. These symmetries have been summarized by Woodward and Lufasso and can be predicted from the tolerance factors of a given compound with the SPUDS¹³ software.

Besides, there are two additional phenomena that can drive to distortions of a different nature. The first one is related to the presence of cationic displacements from the center of the coordination polyhedra. These asymmetric coordination environments are due to the presence of two particular types of cations: d^0 ions such as Ti^{4+} , Nb^{5+} , W^{6+} , etc., or p-block elements containing electronic lone pairs, such as Pb^{2+} , Bi^{3+} , Sn^{2+} , Te^{4+} . In both cases the main cause of such distortion is attributable to a second-order Jahn–Teller distortion (SOJT) due to electronic effects.^{14–16} Another phenomenon is the distortion of the octahedra driven by electronic instabilities of the B-site cation, as occurs in the Ba_2CuTeO_6 ¹⁷ perovskite, where the presence of a first order Jahn–Teller effect (i.e., Cu^{2+} , $3d^9$) induces the distortion of the CuO_6 octahedra generating an elongation of the c -axis.

Many ABO_3 and $A_2B'B''O_6$ perovskites containing p-elements with an electron lone pair at the A positions, exhibiting an irregular oxygen-coordination environment, require the use of high-pressure conditions to be stabilized. Actually, the well-known ferroelectric $PbTiO_3$ is the only Pb-3d transition metal perovskite that can be prepared at ambient pressure, while some other members such as $PbMnO_3$, $PbCrO_3$, or $PbVO_3$ have only been stabilized under elevated pressures.¹⁸ Concerning the double perovskites, two nice examples are Bi_2NiMnO_6 ¹⁹ and Bi_2CoMnO_6 ,²⁰ prepared under pressure, where the presence of a lone pair induces cationic shifts which favor ferroelectricity: these materials are magneto-ferroelectrics, useful for multiple-memory devices (storage of information with both electrical and magnetic polarization), or electrically writable, magnetically readable magnetoelectric random-access memory devices. In some cases the preparation of double perovskites containing p-block ions such as Pb^{2+} or Bi^{3+} is difficult due to the possibility of producing the particularly stable pyrochlore phases which compete with the perovskite complicating the stabilization of a pure phase.

Recently, we have reported on the crystal structure, phase transitions, and dielectric properties of a novel series of double perovskites Pb_2RSbO_6 for $R = Ho, Er, Tm, Yb, \text{ and } Lu$.^{21,22} At room temperature these compounds exhibit a rare and highly distorted crystal structure described in the space group $C2/c$ (No. 15), presenting two different kinds of distortions: a tilting distortion, belonging to the $a^-b^-b^-$ tilt system as defined by Woodward,¹³ and the existence of an intraoctahedral distortion due to the displacement of the R atom from the center of its octahedron along a C_2 axis, which seems to be related to an asymmetric interaction between oxygen atoms and Pb. These atoms show an important shifting of $\approx 0.5\text{--}0.6$ Å. Moreover, depending on the lanthanide ionic radii, these phases can show three successive phase transitions following the sequence $C2/c \rightarrow P2_1/n (i_1) \rightarrow R\bar{3} \rightarrow Fm\bar{3}m$ (when $R = Tm, Yb, \text{ and } Lu$) or two successive transitions $C2/c \rightarrow P2_1/n (i_2) \rightarrow Fm\bar{3}m$ for Ho and Er, where $P2_1/n (i_1)$ and $P2_1/n (i_2)$ stand for commensurate subcells of more complex incommensurate structures.

In order to clarify the nature of the distortion of the room temperature crystal structure of the compounds of this family and to compare the effect of the replacement of Ln ($4f^n$) by a d^0 transition metal we have synthesized the yttrium derivative and studied the thermal evolution of its crystal structure from 100 to 500 K. Moreover, the absence of f-electrons has simplified the study of the electronic structure by using DFT calculations, giving important insights on the actual role of the $6s^2$ lone pair of lead.

EXPERIMENTAL SECTION

Pb_2YSbO_6 (PYSO) was obtained by standard solid-state techniques; PbO , Y_2O_3 , and Sb_2O_3 were used as starting materials. They were weighed out in the appropriate metal ratios and well-mixed in an agate mortar. The mixture was calcined at 550 °C for 24 h in order to oxidize Sb^{3+} to Sb^{5+} . Subsequently, the product was heated at 800 and 900 °C for 12 h until a single Pb_2YSbO_6 phase was obtained. All the thermal treatments were carried out in sintered alumina crucibles and in air atmosphere. After all the calcination steps the sample was cooled down by switching off the furnace.

The initial structural identification and characterization of PYSO was carried out by laboratory XRPD ($Cu K\alpha$, $\lambda = 1.5406$ Å) in a Bruker D8 Advance powder diffractometer with the Bragg–Brentano geometry. In addition, NPD data were collected in the D1A high-resolution diffractometer ($\lambda = 1.910$ Å) at ILL, Grenoble, France. About 4 g of sample was placed in a vanadium can, and the counting time was typically 4 h per pattern. Room temperature and 423 and 523 K patterns were collected in air atmosphere.

The sequential temperature dependence of the crystal structure was studied by using synchrotron X-ray diffraction (SXRD) in the temperature range $100 < T < 550$ K. These experiments were carried out at the Powder Diffraction Station of the Materials Sciences (MS-Powder) beamline at the Swiss Light Source,²³ with the use of the Microstrip Detector Mythen-II. The diffraction patterns were collected between 100 and 550 K with the powder sample enclosed in a glass capillary with a diameter of 0.3 mm. The X-ray wavelength was $\lambda = 0.49049$ Å.

The refinements of the crystal structures were performed by the Rietveld method using the Fullprof Suite.²⁴ The profile of the peaks was fitted by the Thompson–Cox–Hastings pseudo-Voigt function corrected for axial divergence asymmetry. The following parameters were refined in the final run of the fits for the NPD data: scale factor, background coefficients, zero-point error, pseudo-Voigt corrected for asymmetry parameters, positional coordinates, isotropic displacement parameters, occupancy factors for Pb and O atoms, and antisite disordering between Y and Sb atoms. The neutron coherent scattering lengths for Pb, Sb, Y, and O are 9.405, 5.57, 7.75, and 5.803 fm, respectively. Taking into account that the presence of absorption of neutrons/X-rays could affect the isotropic thermal factors of the atoms and therefore the crystal structure determination, absorption effects were included in the refinements; estimated μ coefficients of 0.8 and 0.023 cm^{-1} were considered for X-rays and neutrons, respectively.

The differential scanning calorimetry (DSC) study was performed in a Mettler TA3000 system equipped with a DSC30 unit. The measurements have been carried out during the heating and cooling runs from RT to 523 K with rates of 5, 7, and 10 K min^{-1} for the powder sample encapsulated in a standard Al crucible.

Quantum-mechanical calculations were carried out for the room temperature polymorph of PYSO by means of the periodic density functional theory (DFT). The DF plane-wave calculations were carried out by means of the VASP package^{25,26} considering spin-polarization and dipole corrections explicitly. The total energy was computed using the revised Perdew–Burke–Ernzerhof GGA (RP)^{27,28} exchange-correlation function, using the spin-interpolation formula of Vosko–Wilk–Nusair (VWN).²⁹ The effect of the core electrons on the valence electron density was described by the project or augmented wave (PAW) method.^{30,31} The cutoff for the kinetic energy of the plane-waves was set to 415 eV throughout, which after extensive

testing proved to ensure a total energy convergence better than 10^{-4} eV. A Gaussian smearing technique with a 0.2 eV width was applied to enhance convergence, but all energies presented in the following were obtained by extrapolating to zero smearing (0 K). Integration in the reciprocal space was carried out using the Monkhorst Pack³² with three k -points in the Brillouin zone. The convergence with respect to the number of k -points was better than that of the cutoff energy. The VESTA program³³ was used to visualize and represent the structures of interest and the electron localization.

RESULTS

Pb_2YSbO_6 (PYSO) was obtained as a light yellow powder, and the XRPD pattern was indexed in a perovskite superstructure with unit cell parameters related to the ideal cubic perovskite aristotype ($a_0 \approx 4 \text{ \AA}$) as $a \approx c \approx \sqrt{6}a_0$, and $b \approx \sqrt{2}a_0$ (see Figure 1). The systematic extinctions were consistent with the

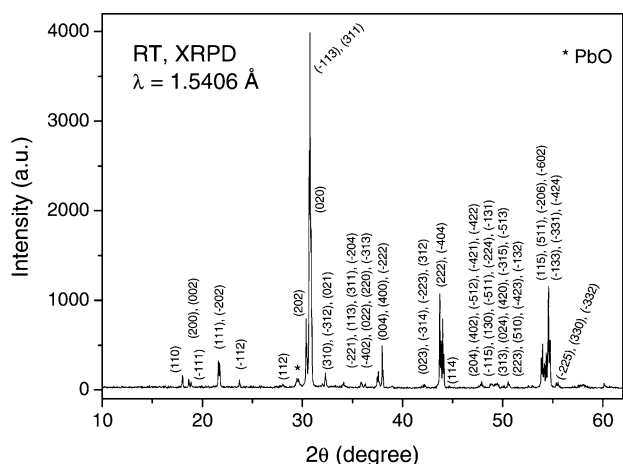


Figure 1. X-ray diffraction pattern XRD of Pb_2YSbO_6 at 300 K, indexed in a monoclinic $C2/c$ (No. 15) unit cell. The star indicates a PbO impurity.

$C2/c$ space group (No. 15),³⁴ and the unit cell parameters showed values close to the previously reported for the compounds Pb_2RSbO_6 with $R = \text{Ho}$ and Er in agreement with the ionic radii similitude between the R cations.

Differential Scanning Calorimetry (DSC). Regarding the known phase transitions present in the thermal evolution of the previously reported members of this family, we performed several DSC measurements for PYSO. The curves obtained at three different heating (cooling) rates (5, 7, and 10 K/min) are

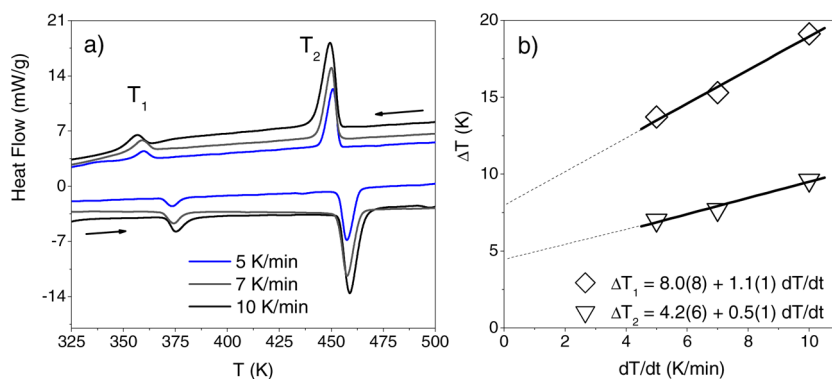


Figure 2. (a) DSC curves measured in a heating/cooling cycle at three different heating/cooling rates: 5, 7, and 10 K/min. (b) Lineal regressions fits for the maxima/minima hysteresis as a function of the heating/cooling rate for both thermal events.

displayed in Figure 2a, and no weight losses were observed after a heating/cooling cycle. Two different endothermic (exothermic) events can be observed on heating (cooling), probably related with two structural transitions which occur in $\text{Pb}_2\text{HoSbO}_6$, the transition temperatures being $T_1 = 375 \text{ K}$ and $T_2 = 459 \text{ K}$. Besides, from the integrated areas below the peaks the transition enthalpies and entropies were $\Delta_1H = 662 \text{ J/mol}$ and $\Delta_2H = 3247 \text{ J/mol}$; $\Delta_1S = 1.8 \text{ J/K mol}$ and $\Delta_2S = 7.3 \text{ J/K mol}$. The extrapolation at zero heating rate shows thermal hysteresis for both events (see Figure 2b).

Neutron Powder Diffraction Study (NPD). Three neutron diffraction patterns were collected at 300, 423, and 523 K, in order to analyze the crystal structure after each thermal event observed by DSC. From them, we confirmed that both peaks are associated with structural phase transitions, showing the same polymorphic sequence than that observed for $\text{Pb}_2\text{HoSbO}_6$:²² $C2/c \rightarrow P2_1/n (i_2) \rightarrow Fm\bar{3}m$. The Rietveld fits are shown in Figure 3a–c, and the unit cell parameters, thermal

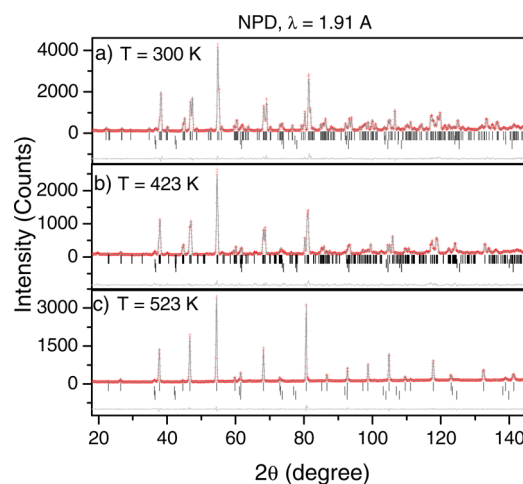


Figure 3. Observed (circles), calculated (solid line), and difference (bottom) profiles after a Rietveld refinement of the NPD data for (a) P_α polymorph of Pb_2YSbO_6 measured at 300 K, (b) P_β polymorph measured at 423 K, and (c) P_γ polymorph measured at 523 K. The second rows of ticks correspond to the PbO impurities with a weight fraction of less than 2%.

factors, and main bond lengths and angles are shown in Tables 1 and 2. From now on the $C2/c$, $P2_1/n (i_2)$, and $Fm\bar{3}m$

structures will be named as P_α (alpha), P_β (beta), and P_δ (delta) polymorphs, respectively.

Table 1. Unit Cell, Positional, and Displacement Parameters and Reliability Factors Obtained from the Refinements of the NPD Data for the α , β , and δ Polymorphs of PYSO from NPD at 300, 423, and 523 K, Respectively

	P_α	P_β	P_δ
space group	C2/c	$P2_1/n$	$Fm\bar{3}m$
a (Å)	10.197 16(2)	8.2992(2)	8.347 69(1)
b (Å)	5.838 58(1)	5.8614(1)	8.347 69(1)
c (Å)	10.166 77(2)	5.9268(1)	8.347 69(1)
β (deg)	108.6843(1)	90.233(2)	90.00
V (Å ³)	573.40(1)	288.31(1)	581.70(2)
R_p	8.65	18.5	12.1
R_{wp}	8.95	17.7	11.0
R_{exp}	6.95	8.4	7.75
R_{BRAGG}	4.48	8.5	2.24
χ^2	1.66	4.4	2.02
Pb	8f	4e	32f
x	0.1317(1)	0.256(1)	0.236(5)
y	0.7822(2)	0.509(2)	0.236(5)
z	0.1263(2)	-0.008(1)	0.236(5)
B_{iso} (Å ²)	1.00(3)	2.3(1)	2.8(4)
Y	4e	2a	4a
x	0	0	0
y	0.2522(4)	0	0
z	$1/4$	0	0
B_{iso} (Å ²)	0.21(2)	0.2(1)	0.9(1)
Sb	4c	2d	4b
x	$1/4$	$1/2$	$1/2$
y	$1/4$	0	0
z	0	0	0
B_{iso} (Å ²)	0.15(4)	0.2(1)	0.3(1)
O1	8f	4e	24e
x	0.1026(2)	0.033(2)	0.2649(2)
y	0.2108(4)	0.257(2)	0
z	0.0888(2)	0.731(2)	0
B_{iso} (Å ²)	0.67(4)	1.2(2)	3.7(3)
O2	8f	4e	
x	0.1470(2)	0.763(1)	
y	0.0375(4)	0.483(3)	
z	0.8516(3)	0.545(1)	
B_{iso} (Å ²)	0.87(4)	1.4(2)	
O3	8f	4e	
x	0.3449(2)	0.018(2)	
y	0.0160(5)	0.726(3)	
z	0.6150(2)	0.749(3)	
B_{iso} (Å ²)	0.75(2)	3.3(4)	

α Polymorph (P_α). Pb_2YSbO_6 is isostructural with the Pb_2HoSbO_6 compound at room temperature. Figure 3a shows the Rietveld refinement of the RT neutron diffraction pattern. The atomic positions of the atoms in the C2/c structural model are shown in Table 1. In this model there are four Pb_2YSbO_6 chemical formulas per unit cell ($Z = 4$). The unit cell parameters obtained were $a = 10.197 16(2)$ Å, $b = 5.838 58(1)$ Å, $c = 10.166 77(2)$ Å, and $\beta = 108.6843(1)^\circ$. In P_α , each YO_6 octahedron is surrounded by six SbO_6 octahedra and vice versa; in fact the alternating YO_6 and SbO_6 units display antiphase tilting along the [100], [010], and [001] directions of the pseudocubic cell.

Table 2. Main Interatomic Distances (Å) and Angles (deg) Obtained for All the Polymorphs at 300, 423, and 523 K

	P_α	P_β	P_δ
Pb Polyhedron			
Pb–O1	3.361(3)*	2.83(2)	3.10(4)
Pb–O1	2.534(3)	2.63(2)	3.10(4)
Pb–O1	2.673(2)	3.22(2)*	3.10(4)
Pb–O1	3.298(2)*	3.12(2)	3.10(4)
Pb–O2	3.212(4)*	3.18(1)	2.96(4)
Pb–O2	3.105(3)	2.75(1)	2.96(4)
Pb–O2	2.481(4)	2.91(2)	2.96(4)
Pb–O2	2.882(3)	2.98(2)	2.96(4)
Pb–O3	2.507(3)	2.75(2)	2.80(4)
Pb–O3	2.977(3)	2.89(2)	2.80(4)
Pb–O3	3.100(3)	3.08(2)	2.80(4)
Pb–O3	3.375(3)*	3.07(2)	2.80(4)
⟨Pb–O⟩	2.782	2.926	2.953
YO_6 Polyhedron			
Y–O1 (×2)	2.222(2)	2.21(1)	2.211(2)
Y–O2 (×2)	2.277(3)	2.20(1)	2.211(2)
Y–O3 (×2)	2.196(3)	2.19(2)	2.211(2)
⟨Y–O⟩	2.232	2.20	2.211
O1–Y–O1	167.5(2)	180	180
O2–Y–O2	84.0(1)	90	90
O3–Y–O3	104.0(1)	90	90
O2–Y–O3	168.2(2)	87.6(9)	90.0
SbO_6 Polyhedron			
Sb–O1 (×2)	1.999(2)	1.994(12)	1.962(2)
Sb–O2 (×2)	1.975(3)	1.986(11)	1.962(2)
Sb–O3 (×2)	1.998(3)	1.988(18)	1.962(2)
⟨Sb–O⟩	1.991	1.99	1.962
Angles around Sb and O			
O1–Sb–O1	180.0	180.0	180.0
O2–Sb–O2	180.0	180.0	180.0
O3–Sb–O3	180.0	180.0	180.0
O2–Sb–O3	89.9(2)	90.2(9)	90.0
Y–O1–Sb	157.0(1)	164.8(5)	180.0
Y–O2–Sb	157.7(1)	164.5(4)	180.0
Y–O3–Sb	164.0(1)	170.3(7)	180.0
θ_A	-11.3	-7.7	0
θ_B	-9.7	-6.2	0
θ_C	-9.6	-6.3	0

*Disregarded value.

β Polymorph (P_β). The structural determination of the P_β polymorph has been carried out at 423 K from neutron powder diffraction data, in the plateau after the first DSC peak. The best indexing of the β polymorph pattern was achieved in the monoclinic system, space group $P2_1/n$ (No. 14), $Z = 2$ (Figure 3b). The unit cell parameters were $a = 8.2992(2)$ Å, $b = 5.8614(1)$ Å, $c = 5.9268(1)$ Å, and $\beta = 90.233(2)^\circ$, which are related with the a_0 lattice constant of the aristotype as $b \approx c \approx \sqrt{2}a_0$ and $a \approx 2a_0$. The atomic positions in this model are given in Table 1. This is a commensurate subcell of a more complex incommensurate structure: as it was observed and detailed for other family members, some small peaks (only appearing between T_1 and T_2) have been observed in the neutron diffraction pattern but they were not fitted by the mentioned model, suggesting the presence of a modulation in the structure. Regarding the synchrotron data, there are several tiny peaks in the whole pattern; the positions of these peaks in the XRD patterns do not show a complex thermal evolution,

unlike that observed for the R = Lu, Yb, and Tm compounds, which show a strong thermal dependence. An averaged description of the crystal structure can be performed taking into account a $P2_1/n$ structure, describing very satisfactorily all the remaining peaks in the pattern; we could assume that these unsolved peaks are indicating the presence of a modulation in the commensurate $P2_1/n$ subcell. Upon the careful determination of all the extra peak positions, these were subjected to an exhaustive search for the possible propagation vector of the incommensurate modulation. This has been done with the help of the program *k-search* which is a part of the Fullprof Suite of programs and for the pattern collected at 428 K.²⁴ A really fine grid for the search, as well as the outstanding quality in terms of resolution and signal-to noise ratio of the synchrotron X-ray diffraction patterns recorded, did ensure the success of the search, and we have found that all the extra lines are adequately described by the propagation vector $\mathbf{q} = [\sim 0.961, 0, \sim 0.339]$. This vector lies in the a^*-c^* plane of the reciprocal lattice, thus implying that the crystal structure of the β polymorph is modulated in the $a-c$ plane, remaining ideally periodic in the b direction. This modulation vector remains stable in the whole temperature range of the existence of the β polymorph.

A comparison between the refinements of the synchrotron data at 428 K by using only (a) the commensurate subcell and (b, profile-matching mode) adding the wave-vector to the commensurate cell is shown in Supporting Information Figure S.3. The inclusion of the modulation vector allows all extra diffraction lines to be adequately indexed. Supporting Information Table S.1 shows the comparison between the unit cell parameters and reliability factors of both profile fittings. The very fact that these incommensurate structure modulation peaks are very strongly pronounced in the X-ray data compared to the case of neutron powder diffraction patterns, where they are well-observed, but are generally much weaker and not really hindering the secure refinement of the main average crystal structure, indirectly implies that the main underlying mechanism of the structure modulation should involve the displacement of heavier atoms, since exactly these are carrying the main scattering power for X-rays. That is, indirectly we can assume that these are probably the lead atoms, which are subjected to the incommensurately modulated displacements. The determination of the real four-dimensional space group and of the actual detailed crystal structure of all the members of the Pb_2RSbO_6 family, including the Pb_2YSbO_6 perovskite, is currently in progress.

δ Polymorph (P_δ). The last polymorph was found to be a double cubic perovskite structure. The structural refinement of the NPD data was performed at 523 K in the $Fm\bar{3}m$ (No. 225) space group (Figure 3c). In this model, Y and Sb atoms were located at the 4a (0, 0, 0) and 4b ($1/2, 0, 0$) Wyckoff sites, respectively. O atoms are placed along the 24e sites ($x, 0, 0$), and Pb atoms occupy the 32f (x, x, x) positions, presenting a subtle off-center displacement along the [111] direction, similar to that reported for $\text{Pb}_2\text{ScSbO}_6$.³⁵

In order to mimic a sphere-like disorder of Pb atoms around the average ($1/4, 1/4, 1/4$) positions, three structural models including the [100], [110], and [111] shifts of this atom were examined by the Rietveld method adopting the split-atom method, where one Pb atom is assumed to randomly occupy the ($x, 1/4, 1/4$), ($x, x, 1/4$), and (x, x, x) equivalent sites, respectively, around the ($1/4, 1/4, 1/4$) position. During the refinements only the thermal parameter B_{pb} and the x value were allowed to vary. All the structural models led to reasonable

agreement factors, involving important reductions of the displacement parameters of the Pb cations. The best numerical improvement of the *R*-factors was obtained for the model in which the Pb ions statistically occupy the (32f) position (x, x, x), distributed in a sphere with a radius of 0.27 Å (see Supporting Information Table S.2). In this case the temperature factor, B_{pb} , is reduced to 2.8(4) Å². Finally, the oxygen and lead stoichiometry of the samples and the antisite disorder between Y and Sb were checked at the highest temperature, and no deviation from the normal stoichiometric formula Pb_2YSbO_6 was detected within the standard deviations.

DFT Calculations. The electronic structure of the room temperature polymorph of Pb_2YSbO_6 (P_α) has been studied using density functional theory (DFT). For the ground-state crystal structure we directly considered that obtained from our neutron diffraction data experiments at RT. The unit cell volume is 573.40 Å³, and there are six atoms in the asymmetric unit. The total and projected densities of states (DOS) of Pb_2YSbO_6 are shown in Figure 4a, b. The zero energy was arbitrarily taken at the Fermi level.

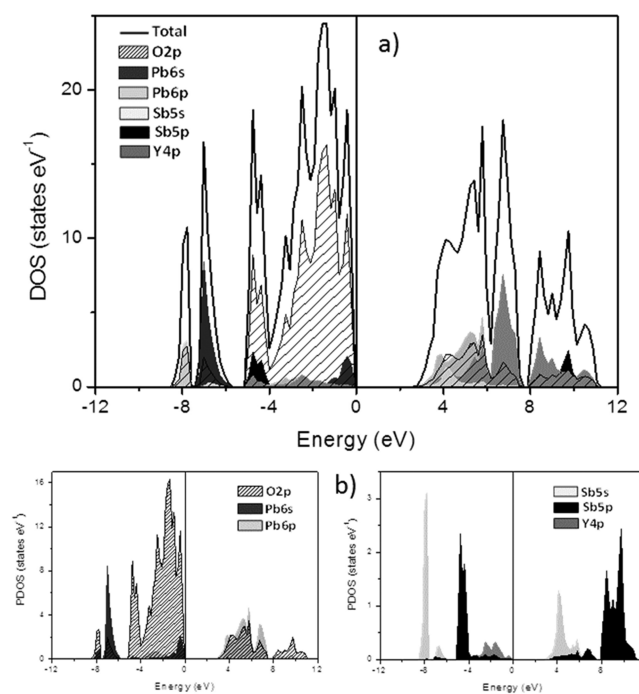


Figure 4. (a) Total and projected density of states (DOS) calculated for the room temperature polymorph (P_α) of PYSO. The parameters were fixed at the values obtained from the refinements of the neutron diffraction data. (b) Separated density of states projected on the different atoms of the structure.

The top of the valence band (VB) and the bottom of the conduction band (CB) are composed of the occupied O 2p states and unoccupied Pb 6p and Y 4d states, respectively. In another perovskite containing lone pair elements, it can be seen that, for example, the band gap of PbZrO_3 (lone pair + 4d metal)³⁶ is determined by occupied O 2p states and unoccupied Zr 4d states rather than those associated with Pb–O, while for BiScO_3 ³⁷ (very similar crystal structure and lone pair + 3d⁰) the main contributions to those regions are the O 2p and Bi 6p states, respectively. It is important to remark that the crystal structure of PbZrO_3 is orthorhombic $Pbam$ ³⁸ while BiScO_3 shows a monoclinic, $C2/c$ structure, like PYSO

but without B-site ordering. The band gap calculated for PYSO was 2.9 eV, in agreement with the insulating nature of the sample.

The yttrium DOSs show some sharp peaks at about -17 eV, which are not shown in Figure 4, and consist of highly localized Y 5p states. The total DOS plot shows sharp peaks between -8.5 and -5.5 eV which are mainly due to O 2p and Pb 6s, and a small contribution of O 2s and Pb 6p. These peak shapes suggest localized states and have been observed several times in oxides containing lone pair elements with strong A–O hybridization, giving rise to the formation of lobe-shaped nonbonded electronic pairs.³⁹ The presence of a small contribution of the 5s states of Sb to the VB can be seen at -8 eV (dashed lines in Figure 4a), which occupies the same region as some O 2p states. Most of the VB states are concentrated between -5 and 0 eV; the top of this band is composed mainly of oxygen 2p states with some contributions from Sb 5p and Y 4d states. In fact, a marked hybridization between O 2p and Sb 5p states is suggested from the analysis of the peaks located between -5.0 and -4.0 eV, giving rise to highly covalent Sb–O bonds, as it was observed for $\text{Pb}_2\text{ScSbO}_6$.³⁵ This will be discussed later from the electronic localization function analysis. On the other hand, the yttrium contribution to the top of the VB is small compared with the contribution to the CB, but it denotes a small hybridization between Y 4d states and O 2p which are responsible of a weak covalent contribution in the Y–O bond.

Crystal Structure Thermal Evolution from Synchrotron XRD. The thermal evolution of the PYSO crystal structure was studied between 100 and 500 K from SXR. Supporting Information Figure S.1.a,b shows the evolution of the low angle region ($4 < 2\theta < 9^\circ$) of the patterns. From this 2θ region both phase transitions are observed at 372 and 468 K in agreement with the DSC events (375 and 459 K, respectively). In the low temperature study (below 375 K), no additional structural distortion was detected, showing a cell volume compression of 0.45%. Rietveld refinements of some selected patterns are shown in Supporting Information Figure S.2, showing a good fit by using the structural models obtained from NPD experiments. A comparison between the refinements with and without the inclusion of the modulation wave-vector is shown at Supporting Information Figure S.3. Supporting Information Figure S.4 shows the thermal evolution of the unit cell volume, parameters, bond lengths, and tolerance factor obtained between 100 K and room temperature. In this region, the thermal expansion coefficient α was calculated for each unit cell parameter, following the procedure reported elsewhere.^{40,41} The obtained values were $\alpha_a = 8.591 \times 10^{-6} \text{ K}^{-1}$, $\alpha_b = 1.456 \times 10^{-5} \text{ K}^{-1}$, and $\alpha_c = 7.683 \times 10^{-6} \text{ K}^{-1}$, showing an important difference between the b thermal expansion coefficient with respect to those of a and c . This issue will be discussed in subsequent sections.

The results obtained for the evolution of the unit cell volume and parameters are presented in Figure 5a,b showing a thermal evolution pattern that agrees with that obtained for the compounds with Ln = Ho, Er, Tm, Yb, and Lu. In this case the b parameter shows a steady expansion with increasing temperature from 100 K through the first phase transition, showing a discontinuity at T_2 . For the c parameter a contraction of 0.35% is observed at T_1 , reaching a value even smaller than the room temperature one, while a marked expansion occurs at the second phase transition. Finally, a shows an important

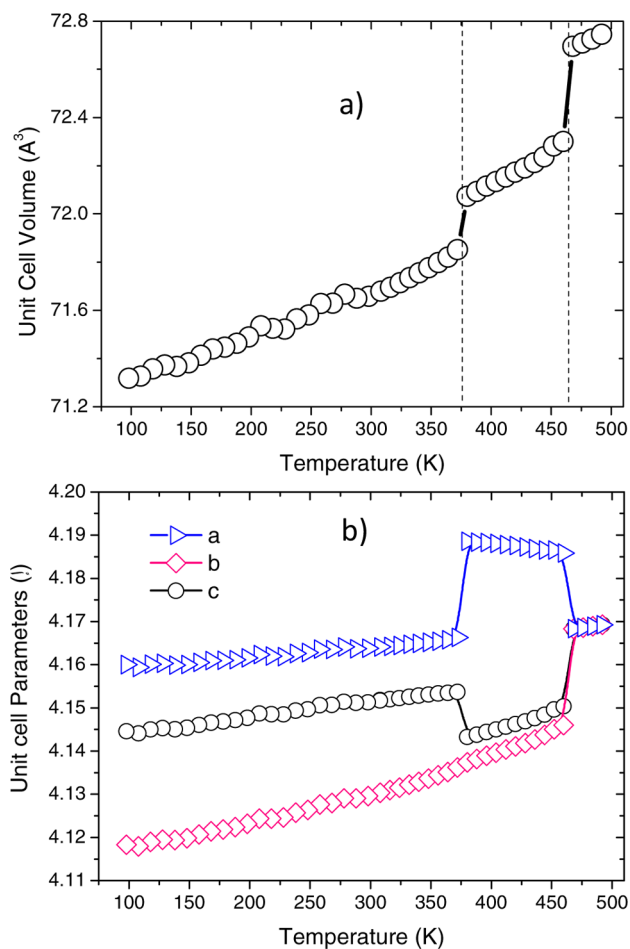


Figure 5. (a) Thermal evolution of the unit cell volume and (b) the unit cell parameters per formula of PYSO across the phase transitions between 100 and 500 K, obtained from the Rietveld refinements of the synchrotron X-ray diffraction data, $\lambda = 0.82658 \text{ \AA}$.

expansion at T_1 with a steady contraction (on heating) between T_1 and T_2 , the temperature at which a new contraction occurs.

The calculation of the thermal expansion coefficients for the different polymorphs gave a nice trend depending on the parameter. Therefore, for P_α the obtained values were close to those observed at low temperature: $\alpha_a = 8.143 \times 10^{-6} \text{ K}^{-1}$, $\alpha_b = 1.588 \times 10^{-5} \text{ K}^{-1}$, and $\alpha_c = 7.808 \times 10^{-6} \text{ K}^{-1}$. The β polymorph shows some interesting changes in the thermal expansion, characterized by $\alpha_a = 2.16 \times 10^{-5} \text{ K}^{-1}$, $\alpha_b = 2.59 \times 10^{-5} \text{ K}^{-1}$, and $\alpha_c = -8.06 \times 10^{-6} \text{ K}^{-1}$, showing a merging of the positive values and the appearance of a negative thermal expansion at the c axis. Finally, for the cubic polymorph, all the thermal expansion coefficients converge to the same α value of $9 \times 10^{-6} \text{ K}^{-1}$.

The thermal evolution of the unit cell volume (Figure 5a) shows the condensed information about the phase transitions in the system. In agreement with the hysteretic nature observed for both events from the DSC experiments, the volume shows two discontinuous expansions, suggesting first order processes at both temperatures.

DISCUSSION

The $C2/c$ monoclinic structure is characterized by the presence of 1:1 cationic ordering between Y(III) and Sb(V) accompanied by out of phase octahedral rotations in all the

crystallographic directions. The magnitude of those tilting angles is shown in Table 2, and it scales with the tolerance factors calculated for the Pb_2RSbO_6 perovskites, with $R = \text{Ho}$, Er , Tm , Yb , and Lu , with the yttrium and the holmium samples being the most distorted ones.

Although the distortion of the RT crystal structure shows octahedral tilting, it must be pointed out that this is not the only distortion present in this case. Moreover, the presence of a lone pair element may affect particularly the crystal structure. For this, it is useful to compare the case of PYSO with a double perovskite with a similar tolerance factor but without a lone pair element like Sr_2YSbO_6 , defined in the $P2_1/n$ space group.⁴² The tolerance factors of Pb_2YSbO_6 and Sr_2YSbO_6 calculated from the ionic radii sums are $t_p = 0.950$ and $t_s = 0.934$, respectively, suggesting that the strontium sample should present the most distorted structure. The average tilting angle calculated for Sr_2YSbO_6 ⁴² was 12.0° , while for Pb_2YSbO_6 it was 10.2° , as expected from the t values. However, by comparing both structures the one defined in $C2/c$ seems to be more distorted than the $P2_1/n$ one; moreover, the next stage on the thermal evolution of PYSO is an incommensurated $P2_1/n$ structure. From the observed data it seems that the sum of the contributions of a small tolerance factor and the presence of an important covalent effect in the Pb–O bonds (see the DOS plots at Figure 4) is inducing a higher crystal distortion in the case of Pb_2YSbO_6 with respect to Sr_2YSbO_6 , even when the second one has a smaller tolerance factor.

As it was mentioned, there are two different features related with the lead and the yttrium coordination polyhedra. Figure 6

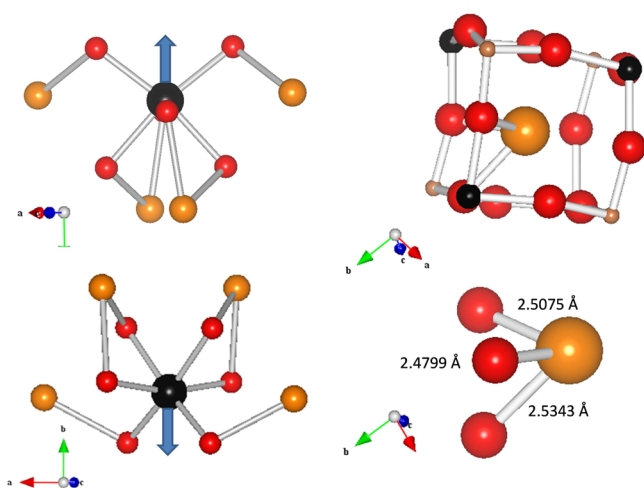


Figure 6. Schematic view highlighting the displacement of the yttrium atoms (black spheres) and lead atoms (orange spheres) in the void between eight octahedra for the α polymorph where the lead atom environment generated by the three shorter Pb–O bond distances is shown.

shows the Y and Pb environment at RT, plotted from the structural data of Table 2, and it highlights a shift of yttrium atoms along one of the octahedral $C2$ directions of 0.17 \AA . Moreover, the lead polyhedron is highly distorted, showing an 8-fold coordination plus a 0.60 \AA displacement of the metallic atom from the center. These atomic shifts are characterized by a group of three short Pb–O bond lengths, the shortest being $2.481(4) \text{ \AA}$, and two short Y–O bond distances (see Table 2). The displacement of Pb atoms has been previously observed in several compounds and it has been related⁴³ to the appearance

of a strong hybridization between the Pb 6s and 6p and O 2p states, giving rise to an occupied nonbonded orbital located at the opposite direction of the shifting (where the strong Pb–O interaction occurs).

In a comparison of this compound with some of the previously reported Pb_2RSbO_6 with $R = \text{rare earths}$ we have found no big influence of the 4f level electronic filling. In fact, the main differences observed for the compounds of this family are related to the ionic radii of the rare earth. As it can be seen in Supporting Information Figure S.5, the unit cell parameters scale with the rare-earth ionic size. Moreover, the yttrium compound shows the same crystal structure evolution as that of the previously reported samples with $R = \text{Ho}$ and Er (the ionic radii of these cations in octahedral coordination are 0.89 , 0.901 , and 0.90 for Er , Ho and Y , respectively) where the modulation characteristic of the β polymorph is temperature independent while for the samples with $R = \text{Lu}$, Yb , and Tm the modulation is highly temperature dependent. Regarding the transition temperatures, they do not follow the same trend shown by the rare earth compounds, which is reasonable since the covalent component to the B–O bond is higher for yttrium than for the other lanthanides.

As we described in the Results section, from the density of state calculations we have found evidence about the presence of several hybridizations between Pb–O, Sb–O, and Y–O. Figures 7 and 8 show different views of the electronic

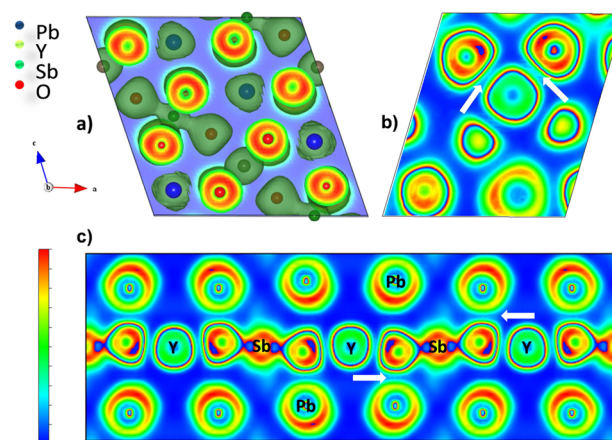


Figure 7. Schematic representation of the electron localization function of different views of the room temperature polymorph (α) crystal structure: (a) (010) plane containing Pb, Y, Sb, and O atoms, (b) (110) 2D cut, and (c) projection along the (101) direction. The white arrows indicate a small electronic density between two atoms.

localization functions (ELFs) obtained for the octahedra of the P_α structure. From there, we can point out the pronounced electronic differences that exist between SbO_6 and YO_6 octahedra, showing the former one a higher electronic density at the internuclear region while for the yttrium octahedra the electronic density is located mainly on the oxygen atoms. This great difference is related to the hybridization between the Sb 5p and O 2p states (see Figure 4) and could give a nice trace about the nature of the driving force for the cationic ordering in the perovskite structure, as occurs in $\text{Pb}_2\text{ScSbO}_6$.³⁵

Paying attention to the electronic density distribution near lead atoms, a lobe of high electronic density can be seen in the region opposite to the atomic shifting, which seems to be responsible for the irregular oxygen positions in that region.

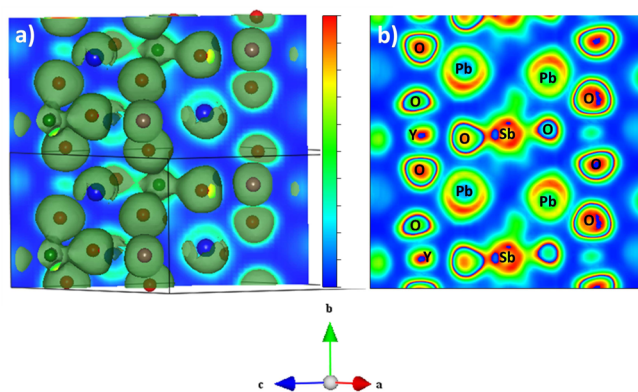


Figure 8. Schematic representation of the electron localization function obtained for the room temperature polymorph (α) of the (201) plane. Left picture shows a 3D representation while the picture on the right shows a 2D cut of the plane with an isosurface of 0.2912. The antiferroelectric ordering of the nonbonded electronic pair can be clearly seen.

These lobes are the nonbonded electronic pairs of Pb^{2+} ions. Figure 8 shows that these lobes are arranged giving rise to an antiferroelectric ordering along the b monoclinic axis. This kind of behavior has been observed previously in oxides containing lone pair elements, like Pb(II) , Sn(II) , or Bi(III) ,^{44,45} and it is related to the hybridization between $\text{Pb } 6s$ and $6p$ states with $\text{O } 2p$ ones. Moreover, this shifting generates an asymmetric $\text{Pb}-\text{O}$ interaction and affects directly the yttrium polyhedron. In fact, taking a close view of the structure, it can be seen that yttrium is shifted away from the strong $\text{Pb}-\text{O}$ bonds, which suggests the presence of a chemical or electronic pressure of Pb through some oxygen atoms to yttrium, generating an asymmetric YO_6 unit.

In the case of Sb , the nature of the $\text{Sb}-\text{O}$ bond seems to be hard to modify, in agreement with the polarizability values of these atoms, keeping it virtually unchanged; moreover the $\text{Pb}-\text{O}_n-\text{Sb}$ interaction is symmetrical, while the $\text{Pb}-\text{O}-\text{Y}$ is not. A nice comparison can be carried out analyzing the plane shown at Figure 7c. In this figure a chain $\text{O}-\text{Sb}-\text{O}-\text{Y}-\text{O}$ is represented, and the interactions with lead atoms are highlighted. Notice that lead atoms present the lone pair located in the opposite direction of the short $\text{Pb}-\text{O}$ bond lengths. In the case of Sb , the short $\text{Pb}-\text{O}$ bond lengths are alternating (above and below the Sb atom), while in the case of Y , both Pb atoms show the short bond length below the $\text{O}-\text{Y}-\text{O}$ line. In fact, this asymmetry seems to push the Y atoms away from the center of the octahedron, while Sb remains at the center. In fact, the ELF of the YO_6 octahedron (see Figure 7b) shows the presence of a small electron transfer between Y and the two oxygen atoms toward which the displacement occurs. This issue was expected, since the DOS results showed the presence of $\text{Y } 4d$ states in the valence band, partially sharing the energy region with oxygen $2p$ states.

Going back to the P_α crystal structure, we determined from Supporting Information Figure S.4.c the thermal expansion coefficients $\alpha_a = 8.143 \times 10^{-6} \text{ K}^{-1}$, $\alpha_b = 1.588 \times 10^{-5} \text{ K}^{-1}$, and $\alpha_c = 7.808 \times 10^{-6} \text{ K}^{-1}$ along a , b , and c directions of the cell, respectively. The thermal evolution of the bond lengths shows that the main component of the cell compression is related to the $\text{Pb}-\text{O}$ bond lengths, while the $\text{Y}-\text{O}$ and $\text{Sb}-\text{O}$ bonds stay unchanged on average, which agrees with the fact that the AO_x

polyhedron in perovskites is usually more compressible than the BO_6 octahedron, in the absence of electronic effects.

Another interesting fact here is that the thermal expansion coefficient along the b direction is almost 2 times bigger than that calculated along a and c axes, which could be related to the yttrium shift which occurs parallel to the b axis, probably giving some flexibility to the structure plus the marked difference in $\text{B}-\text{O}-\text{B}$ angles. These angles take the values 157.0° , 157.7° , and 164.0° , for O1 , O2 , and O3 , respectively. Moreover, the angle around O3 has a non-negligible component on the b direction, and it is capable of decreasing its value, contributing in this way to a higher thermal expansion coefficient on this direction. Finally, the electronic nonbonded pair of lead is directed along the b direction (Figure 8), which is associated to a bigger magnitude of the $\text{B}-\text{O}-\text{B}$ bond angle across this direction and hence to a higher thermal expansion coefficient.

For the incommensurately modulated crystal structure of the β polymorph, we have determined that its modulation vector $\mathbf{q} = [\sim 0.961, 0, \sim 0.339]$ is temperature-independent in the whole range of existence of the β phase, similar to the case of $\text{Pb}_2\text{HoSbO}_6$. This feature constitutes the main difference between the incommensurate structures of the β polymorphs in the family (named $\text{P}2_1/n (i_1)$ and $\text{P}2_1/n (i_2)$ in ref 22), since the compounds with the biggest tolerance factors ($R = \text{Lu}$, Yb , and Tm) show a strong thermal dependence of the modulation while the Ho and Y ones are temperature-independent. The Er compound phenomenology is more complicated, and it shows a breaking point in the series, since there is an additional transition from a temperature-independent to a temperature-dependent modulation. The smooth connection found between both kinds of modulations suggests that the tolerance factor (degree of structural distortion) drives the transitions and determines the thermal evolution of each particular compound. However, it is important to take into account that the driving force for this peculiar structural behavior could be strongly influenced by the effect of the lead lone electron pair.

Finally, the crystal structure evolution of this material ends in a cubic double perovskite as detailed in the Results section. This is a completely B-site ordered structure with alternating YO_6 and SbO_6 octahedra along the $[111]$ direction. The refinement of the crystal structure at 523 K gave a very large displacement factor for Pb cations ($B_{\text{Pb}} = 3.64(7) \text{ \AA}^2$) with Pb atoms preliminarily occupying the special $(1/4, 1/4, 1/4)$ positions in agreement with those found in other lead-containing perovskites.^{46–50} Usually, large B -values have been attributed to some static or dynamic structural disorder where Pb cations are locally displaced from its ideal position. The correlation length of these displacements is relatively short, and thus, this effect is incorporated into the displacement parameter during the Rietveld refinement. Lead atoms are rarely found at its idealized special position, but rather statistically distributed over higher-multiplicity sites around it. Since the off-centering of Pb provides a strong dipolar moment, the direction of this shifting is very important. Lone pair electrons in Pb are combined with the formation of short $\text{Pb}-\text{O}$ bonds, caused by the strong Pb polarizability. On average, the Pb atom is off-centered against the O_{12} cage by as much as 0.30 \AA at 523 K. After testing several possibilities, we found very similar and good R_B factors for the three refinements, the most convincing being the one related with the Pb at $32f (x, x, x)$ positions, due to the important reduction of the isotropic thermal factor. Following the procedure reported by Hamilton,⁵¹ we have found there is

no chance to distinguish between the three proposed shifting models, and therefore lead atoms should be analyzed as atoms randomly distributed in a sphere of radius 0.27 Å, around the special position ($1/4, 1/4, 1/4$), as observed in other examples of double perovskites. Quite possibly, the observed disorder could be associated with the location of the nonbonded electronic pair in the corresponding cage.

CONCLUSIONS

In this work we have synthesized and analyzed the crystal structure, thermal evolution, and electronic structure of Pb_2YSbO_6 . This material shows a complex temperature dependence of the crystal structure, showing two consecutive first order phase transitions. The structural sequence is the same as those observed for the lower tolerance factor members of the family ($R = \text{Ho}$), being $C2/c \rightarrow P2_1/n (i2) \rightarrow Fm\bar{3}m$. The α polymorph structure is highly distorted and very rare, the members of the Pb_2RSbO_6 family being the only double perovskites reported to exhibit it. The intermediate temperature structure of the β polymorph may be viewed as an incommensurately modulated monoclinic double perovskite with the a^-b^+ system of tilts. Its modulation is adequately described by the modulation vector $\mathbf{q} = [\sim 0.961, 0, \sim 0.339]$, implying the main underlying structural modulation effects to have the periodicity solely in the $a-c$ plane. Finally, after the last phase transition the material shows a cubic B-site ordered crystal structure which is mainly characterized by the presence of a Pb atom off-centering. It seems that all the polymorphic phases show a strong influence of the Pb electron pair, with the main features of the structures related to its occurrence.

The density of states and electronic localization functions revealed the presence of covalent interactions between Pb 6s and 6p states with oxygen 2p states, which gives rise to the lobe-shaped electron pair. These interactions generate a highly asymmetric environment for lead atoms due to cationic displacements. Moreover, it seems that lead displacement pushes the empty Y 4d states to the valence band and induces the appearance of a small hybridization with the O 2p orbitals. This hybridization results in a small shifting of the Y cation along the $C2$ local octahedral direction. Finally, a strong covalent interaction was observed between Sb 5p states and O 2p states, which was expected since this cation usually forms covalent bonds to oxygen.

ASSOCIATED CONTENT

Supporting Information

Temperature dependent SXRD patterns, Rietveld refinement plots, temperature dependence of unit cell parameters, and close up of SXRD patterns. Crystallographic data in CIF format. Tables of data in TXT format. This material is available free of charge via the Internet at <http://pubs.acs.org>.

AUTHOR INFORMATION

Corresponding Author

*E-mail: salarreg@unsl.edu.ar.

Notes

The authors declare no competing financial interest.

ACKNOWLEDGMENTS

S.A.L. acknowledges a CONICET fellowship. J.C.P. acknowledges CONICET (Project PIP 2008-01360) and SECyT-UNSL (Projects 7707 and 2-1612). J.C.P. is member of

CONICET. J.A.A. acknowledges the financial support of the Spanish Ministry of Education to Project MAT2010-16404. The work is partially based on the results of experiments carried out at the Swiss Light Source, Paul Scherrer Institut, Villigen, Switzerland, and experiments carried out at the Institut Laue-Langevin, Grenoble, France. V.A.P.O. acknowledges financial support from the MCYT in the Ramon y Cajal Program and ENE2009-09432. Computational time has been provided by the Centre de Supercomputació de Catalunya (CESCA) and the Centro de Supercomputación de Galicia (CESGA).

REFERENCES

- (1) Howard, C. J.; Kennedy, B. J.; Woodward, P. M. *Acta Crystallogr., Sect. B* **2003**, *59*, 463–471.
- (2) Sleight, W.; Gillson, J. L.; Bierstedt, P. E. *Solid State Commun.* **1975**, *17*, 27–28.
- (3) Cox, D. E.; Sleight, A. W.; Moon, R. M. *Proc. Conf. Neutron Scattering*; National Technical Information Service: Springfield, VA, 1976; p 45.
- (4) Akbas, M. A.; Davies, P. K. *J. Am. Ceram. Soc.* **1998**, *81*, 670–676.
- (5) Reaney, I. M.; Colla, E. L.; Setter, N. *Jpn. J. Appl. Phys.* **1994**, *33*, 3984–3990.
- (6) Kobayashi, K.-I.; Kimura, T.; Sawada, H.; Terakura, K.; Tokura, Y. *Nature (London)* **1998**, 395677.
- (7) Goldschmidt, V. M. *Die Gesetze der Krystallochemie. Die Naturwissenschaften* **1926**, *21*, pp 477–485.
- (8) Shannon, R. D. *Acta Crystallogr., Sect. A* **1976**, *32*, 751–767.
- (9) Goodenough, J. B.; Zhou, J.-S. *Struct. Bonding (Berlin)* **2001**, *98*, 17.
- (10) Goodenough, J. B.; Kafalas, J. A.; Longo, J. M. *Preparative Methods in Solid State Chemistry*; Academic: New York, 1972; Chapter 1.
- (11) Mao, H. K.; Hemley, R. J.; Fei, Y.; Shu, J. F.; Chen, L. C.; Jephcoat, A. P.; Wu, Y. *J. Geophys. Res.* **1991**, *96*, 8069–8075.
- (12) Katrusiak, A.; Ratuszna, A. *Solid State Commun.* **1992**, *84*, 435–441.
- (13) Lufaso, M. W.; Woodward, P. M. *Acta Crystallogr., Sect. B* **2001**, *57*, 725–738.
- (14) Pearson, R. G. *J. Am. Chem. Soc.* **1969**, *91*, 4947–4955.
- (15) Pearson, R. G. *THEOCHEM* **1983**, *103*, 25–34.
- (16) Wheeler, R. A.; Whangbo, M.-H.; Hughbanks, T.; Hoffmann, R.; Burdett, J. K.; Albright, T. A. *J. Am. Chem. Soc.* **1986**, *108*, 2222–2236.
- (17) Iwanaga, D.; Inaguma, Y.; Itoh, M. *J. Solid State Chem.* **1999**, *147*, 291–295.
- (18) Oka, K.; Azuma, M.; Hirai, S.; Belik, A. A.; Kojitani, H.; Takano, M.; Shimakawa, Y. *Inorg. Chem.* **2009**, *48*, 2285–2288.
- (19) Azuma, M.; Takata, K.; Saito, T.; Ishiwata, S.; Shimakawa, Y.; Takano, M. *J. Am. Chem. Soc.* **2005**, *127*, 8889–8892.
- (20) Baettig, P.; Spaldin, N. A. *Appl. Phys. Lett.* **2005**, *86*, 012505–8.
- (21) Larrégola, S. A.; Alonso, J. A.; Sheptyakov, D.; Alguero, M.; Muñoz, A.; Pomjakushin, V.; Pedregosa, J. C. *J. Am. Chem. Soc.* **2010**, *132*, 14470–14480.
- (22) Larrégola, S. A.; Alonso, J. A.; Sheptyakov, D.; Alguero, M.; Muñoz, A.; Pomjakushin, V.; Pedregosa, J. C. *Inorg. Chem.* **2011**, *50*, 5545–5557.
- (23) <http://sls.web.psi.ch/view.php/beamlines/ms/pd/index.html>.
- (24) Rodríguez-Carvajal, J. *Physica B* **1993**, *192*, 55–69.
- (25) Kokalj, A. *J. Mol. Graphics Modell.* **1999**, *17*, 176–179.
- (26) Kresse, G.; Furthmüller, J. *Comput. Mater. Sci.* **1996**, *6*, 15–50.
- (27) Kresse, G.; Hafner, J. *Phys. Rev. B* **1993**, *47*, 558–561.
- (28) Perdew, J. P.; Burke, K.; Ernzerhof, M. *Phys. Rev. Lett.* **1996**, *77*, 558–561.
- (29) Zhang, Y.; Yang, W. *Phys. Rev. Lett.* **1998**, *80*, 890–890.
- (30) Vosko, S. H.; Wilk, L.; Nusair, M. *Can. J. Phys.* **1980**, *58*, 1200–1211.
- (31) Blochl, P. E. *Phys. Rev. B* **1994**, *50*, 17953–17979.
- (32) Kresse, G.; Joubert, D. *Phys. Rev. B* **1999**, *59*, 1758–1775.
- (33) Momma, K.; Izumi, F. *J. Appl. Crystallogr.* **2008**, *41*, 653–658.

- (34) Space Group Symmetry. *International Tables for Crystallography*, Vol. A; Hahn, T., Ed.; D. Reidel Publishing Co. for International Union of Crystallography (IUCr): Dordrecht, The Netherlands, 1983; p 177.
- (35) Larrégola, S. A.; Alonso, J. A.; Pedregosa, J. C.; Martínez-Lope, M. J.; Algueró, M.; De La Peña-OShea, V.; Porcher, F.; Illas, F. *Dalton Trans.* **2009**, 28, 5453–5459.
- (36) Singh, D. J. *Phys. Rev. B* **1995**, 52, 12559–12563.
- (37) Li, C.; Wang, Z.; Wang, C. *Phys. B* **2011**, 406, 2028–2032.
- (38) Corker, D. L. *Acta Crystallogr., Sect. B* **1998**, 54, 18–28.
- (39) Seshadri, R.; Baldinozzi, G.; Felser, C.; Tremel, W. *J. Mater. Chem.* **1999**, 9, 2463–2466.
- (40) Hu, J.; Cai, W.; Li, C.; Gan, Y.; Chen, L. *Appl. Phys. Lett.* **2005**, 86, 151915–151918.
- (41) Awad, R.; Abou-Aly, A. I.; Mahmoud, S. A.; Barakat, M. E. *Supercond. Sci. Technol.* **2007**, 20, 401–405.
- (42) Fu, W. T.; Ijdo, D. J. W. *Solid State Commun.* **2005**, 134, 177–181.
- (43) Walsh, A.; Watson, G. W. *J. Solid State Chem.* **2005**, 178, 1422–1428.
- (44) Raulot, J.; Baldinozzi, G.; Seshadri, R.; Cortona, P. *Solid State Sci.* **2002**, 4, 467–474.
- (45) Stoltzfus, M. W.; Woodward, P. M.; Seshadri, R.; Klepeis, J.-H.; Bursten, B. *Inorg. Chem.* **2007**, 46, 3839–3850.
- (46) Ivanov, S. A.; Eriksson, S. G.; Tellgren, R.; Rundlof, H. *Mater. Res. Bull.* **2004**, 39, 2317–2328.
- (47) Ivanov, S. A.; Tellgren, R.; Rundlof, H.; Thomas, N. A.; Ananta, S. *J. Phys.: Condens. Mater.* **2000**, 12, 2393–2400.
- (48) Thomas, N. W.; Ivanov, S. A.; Ananta, S.; Tellgren, R.; Rundlof, H. *J. Eur. Ceram. Soc.* **1999**, 9, 2667–2675.
- (49) Geddo Lehmann, A.; Kubel, F.; Schmid, H. *J. Phys.: Condens. Matter* **1997**, 9, 8201–8212.
- (50) Lampis, N.; Sciau, P.; Geddo-Lehmann, A. *J. Phys.: Condens. Matter* **1999**, 11, 3489–3500.
- (51) Hamilton, W. *Acta Crystallogr.* **1965**, 18, 502–510.